Simulation of W-band radar reflectivity for model validation and data assimilation

Mary Borderies, Olivier Caumont, Clotilde Augros, Emilie Bresson, Julien Delanoë, Vincent Ducrocq, Nadia Fourrié, Tony Le Bastard, Mathieu Nuret

Simulation of W-band radar reflectivity for model validation and data assimilation

M. Borderies[a]*, O. Caumont[a], C. Augros[b], É. Bresson[d], J. Delanoë[c], V. Ducrocq[a], N. Fourrie[a], T. Le Bastard[a], M. Nuret[a]

[a]*CNRM UMR 3589, Météo-France/CNRS, Toulouse, France*

[b]*DSO/CMR, Météo-France, Toulouse, France*

[c]*LATMOS, Guyancourt, France*

[d]*CNRM UMR 3589, Météo-France/CNRS, Toulouse, France, now at Research Institute on Mines and Environment (RIME), Université du Québec en Abitibi-Témiscamingue, Rouyn-Noranda, Québec, Canada*

*Correspondence to: CNRM UMR 3589, Météo-France/CNRS, 42 avenue Gaspard Coriolis, Toulouse, France.

E-mail: mary.borderies@umr-cnrm.fr

This paper describes a reflectivity forward operator developed for the validation and assimilation of W-band radar data into regional Arome (Applications de la Recherche à l'Opérationnel à Méso-Echelle) class Numerical Weather Prediction models. The forward operator is consistent with the Arome ICE3 one-moment microphysical scheme and is devised for vertically pointing radars. A new neighbourhood validation method, called the Most Resembling Column (MRC) method, is designed to disentangle spatial location model errors from errors in the forward operator. This novel method is used to validate the forward operator using data collected in diverse conditions by the airborne cloud radar RASTA (Radar Airborne System Tool for Atmosphere) during a two-month period over a region of the Mediterranean. The MRC method is then applied to retrieve the optimal effective shapes (i.e. the mean axis ratios) of the predicted graupel, snow and pristine ice, by minimising the standard deviation between observations and simulations. The optimal mean axis ratio is approximately 0.7 for snow and 0.8 for graupel. It is shown that treating snow and graupel particles as oblate spheroids with axis ratios close to their optimal values leads to good agreement between the observations and simulations of the ice levels. Conversely, there is a large bias if snow and graupel particles are considered to be either spherical or overly flattened. The results also indicate that pristine ice can be approximated by a sphere, but this conclusion should be taken cautiously since the amount of pristine ice particles is probably overestimated in the ICE3 microphysical scheme.

Key Words: <cloud radar, forward operator, HyMeX, mesoscale convective simulations>

1. Introduction

Clouds are one of the main driving elements in the global water cycle. They play a key role in the Earth's energy balance, climate and weather via their influence on the global radiation budget (Stephens 2005). The need to observe and characterize the vertical distribution and variability of clouds at a global scale was the

This article has been accepted for publication and undergone full peer review but has not been through the copyediting, typesetting, pagination and proofreading process, which may lead to differences between this version and the Version of Record. Please cite this article as doi: 10.1002/qj.3210

starting point of a new generation of Earth observation systems including cloud radars. By acquiring the vertical profiles of cloud properties, millimetre-wavelength radars can fill the gap between traditional meteorological centimetre radars (Lhermitte 1987; Kollias *et al.* 2007), which are insensitive to the smallest particles, and lidars, which are strongly attenuated by optically thick clouds (especially liquid clouds). In addition, compared to low-frequency radars, millimetre-wavelength radars can be deployed much more easily aboard spacecraft and aircraft because they require smaller antennas to provide high spatial resolution measurements.

Cloud radars either operate in the Ka-band, at ≈ 35 GHz, or in the W-band, at ≈ 95 GHz (Moran *et al.* 1998; Kollias *et al.* 2007; Horie *et al.* 2000; Li *et al.* 2001; Wolde and Pazmany 2005; Delanoë *et al.* 2013; Hagen *et al.* 2014). Even though they are more attenuated by heavy precipitation, W-band radars are more sensitive to thin clouds than Ka-band radars at a given emitted power (Leinonen *et al.* 2015). In addition, W-band radars are much smaller because the antenna size decreases with the wavelength. W-band radars are recognised as economic (especially frequency-modulated ones Delanoë *et al.* (2016)), lightweight and compact instruments that accurately characterize clouds and light precipitation (Kollias *et al.* 2007).

Since its launch in 2006, the W-band Cloud Profiling Radar (CPR) on-board the CloudSat spacecraft (Stephens *et al.* 2002) has led to significant improvements in our understanding of the mechanisms linking clouds to climate at global scales. Following this success, the EarthCARE satellite mission (Illingworth *et al.* 2015) is scheduled to be launched in 2019 with a Doppler Cloud Profiling Radar, which will have a 7-dB higher sensitivity due to its lower altitude. In addition, the high sensitivity of W-band radars to cloud microphysical properties makes their data extremely appealing for microphysical parameterization validation and data assimilation in regional Numerical Weather Prediction (NWP) models. However, due to the low revisit time of polar-orbiting satellites, their data are of limited value for km-scale short-range forecasting systems. Nonetheless, recent technological breakthroughs might lead to a deployment of ground-based W-band radar networks. For example, the BASTA radar (Delanoë *et al.* 2016) is a lower-cost radar that can provide high-quality measurements of phenomena such as fog and light precipitation. To prepare for the future operational use of these next-generation radars, data from W-band radar aboard research aircraft are available from several field campaigns (Delanoë *et al.* 2013; Fontaine *et al.* 2014; Protat *et al.* 2016). These airborne radars have the advantage of collecting a large dataset of measurements over land and sea at very fine scales.

The first step towards the use of cloud radar observations for model validation and data assimilation is to design a proper method to compare models with observations. There are two different approaches to achieve such comparisons: either the observations are inverted into model variables (Delanoë and Hogan 2008, Protat *et al.* 2014) or a forward operator is used to transform the model variables into synthetic observations (Haynes *et al.* 2007; Bodas-Salcedo *et al.* 2008; Di Michele *et al.* 2012). Uncertainties are easier to assess and control in the forward approach (Reitter *et al.* 2011). Consequently, in the past few years, several cloud radar forward operators have been developed for model validation and/or data assimilation. Many of them have been applied to NWP models with coarse horizontal resolutions (Bodas-Salcedo *et al.* 2008; Di Michele *et al.* 2012, ≈ 40 km).

Very few studies have been devoted to kilometre-scale models with more elaborate microphysical schemes. Iguchi *et al.* (2012) simulated shipborne and spaceborne W-band radar reflectivity using the Japan Meteorological Agency Nonhydrostatic Model (JMA-NHM) with a horizontal grid of 3 km. The simulated reflectivities were compared against observations for bin and bulk microphysical schemes in a relatively small number of cases (three precipitation events). This study highlighted the difficulty of disentangling the differences due to spatial and temporal mismatches between model forecasts and observations from the differences due to the different microphysical schemes. These errors increase with the spatial resolution. Uncertainties also arise from the forward operator formulation. The relationship between the reflectivity and the model variables is not straightforward, especially at high frequency, because the reflectivity is sensitive to the representation of the hydrometeors (Di Michele *et al.* 2012) and, therefore, to the approximations made in the microphysical scheme.

The primary objective of this paper is to present a cloud radar reflectivity forward operator designed for model validation

and data assimilation at kilometre scales (< 3 km). The current study covers a two-month period with the airborne cloud radar RASTA (Radar Airborne System Tool for Atmosphere) (Bouniol *et al.* 2008, Protat *et al.* 2009, Delanoë *et al.* 2013). This airborne radar can cover large distances over land and sea while having a higher resolution than spaceborne instruments. It is also less sensitive than spaceborne instruments to multiple scattering and nonuniform beam filling due to its much smaller footprint. Even though it was primarily designed for an aircraft configuration, this forward operator is directly adaptable to ground-based radars. The forward operator is consistent with the microphysical scheme used in the high-resolution NWP model Arome (Applications de la Recherche à l'Opérationnel à Méso-Echelle) but can in principle be applied to any kilometre-scale model. To distinguish errors in the operator (e.g. the shape and dielectric properties) from the spatial location errors in the model, a novel neighbourhood validation method, the Most Resembling Column (MRC) method, was developed to evaluate and calibrate forward operators designed for vertically pointing radars.

This paper is organized as follows. In Section 2, the airborne cloud radar RASTA and the NWP model Arome-WMed are described. The cloud radar forward operator is detailed in Section 3. The MRC method devised to validate forward operators is then presented in Section 4. Finally, this new method is applied to calibrate the radiative properties in the forward operator and to assess the vertical consistency of the model simulations.

2. Cloud radar data and model simulations

This study takes advantage of the data collected by the airborne cloud radar RASTA during the HyMeX first Special Observing Period (SOP1), which took place from 5 September to 5 November 2012 over a region of the Mediterranean (Ducrocq *et al.* 2014). The RASTA radar is first described in Section 2.1, and details about the data collected by RASTA during the SOP1 are then given in Section 2.2. The mesoscale Numerical Weather Prediction (NWP) model AROME-WMed is presented in Section 2.3.

2.1. RASTA radar

The airborne cloud radar RASTA is a monostatic Doppler multi-beam antenna system operating at 95 GHz (Bouniol *et al.* 2008, Protat *et al.* 2009, Delanoë *et al.* 2013). The aircraft platform used is the French Falcon 20 research aircraft from the SAFIRE unit (Service des Avions Français Instrumentés pour la Recherche en Environnement). This unique instrument allows the documentation of the microphysical properties and the three components of hydrometeor velocities quasi-continuously in time and at a vertical resolution of 60 m (the pulse width is 400 ns).

RASTA has six Cassegrain antennas: three antennas pointing in three non-collinear directions above and below the aircraft. For each of these six antennas, the integration time is 250 ms. Therefore, as the radar switches from one antenna to another, the time resolution for each antenna is 1.5 s, which is approximately equivalent to 300 m because the horizontal speed of the Falcon 20 is approximately 200 m s^{-1}.

The horizontal resolution is also very high because the antenna beamwidth equals 0.6° and 0.8° for the nadir-pointing and zenith-pointing antennas, respectively. The pulse repetition frequency equals 10 kHz, and therefore the maximum unambiguous distance is 15 km. More details on the RASTA configuration during HyMeX can be found in Bousquet *et al.* (2016).

This study focuses on the reflectivity measured by the zenith- and nadir-pointing antennas. The nadir-pointing antenna is slightly more sensitive than the zenith-pointing antenna. The minimum detectable reflectivity at 1 km is approximately -27 dBZ for the nadir-pointing antenna and -26 dBZ for the zenith-pointing antenna. This sensitivity is similar to that of CloudSat (-30 dBZ, Mitrescu *et al.* 2008).

W-band radars can provide valuable information concerning cloud microphysical properties and light-to-moderate precipitation (Kollias *et al.* 2007). Nonetheless, the signal can be strongly attenuated by heavy precipitation.

2.2. Period of study and radar data

The main goal of the HyMeX first Special Observing Period (SOP1) was to document the heavy precipitation events and flash floods that regularly affect northwestern Mediterranean coastal

areas. During the two-month campaign, approximately 20 rainfall events were documented in France, Italy and Spain (Ducrocq *et al.* 2014). Specifically, the RASTA radar aboard the Falcon 20 collected data during 18 flights in and around mesoscale convective systems.

Data were collected over land (nine flights) and over sea (six flights). In three additional flights, the Falcon 20 flew over mixed areas. In some of these flights, data were also collected over mountains. The entire area covered by the Falcon 20 during the SOP1 is represented by the black lines in Figure 1.

For the SOP1, the nadir antenna was calibrated using the ocean surface return technique (Li *et al.* 2005). The data used for the calibration were collected during one of the Megha-Tropiques field campaigns that took place over the Indian Ocean in 2011 (Fontaine *et al.* 2014). The same calibration constant is used for the SOP1 because the system configurations are similar. The calibration accuracy is approximately 1 dB.

To characterise the set of observed vertical profiles during the two-month campaign, a convective index was defined using the vertical velocity measured by RASTA. A vertical column is assumed to be convective if there are at least eight pixels (above the melting layer) either with a vertical velocity greater than 2 m s^{-1} (updraft) or lower than -3 m s^{-1} (downdraft). Using this index, 14.3% of the observed vertical columns can be defined as convective (17,531 out of 122,403). This proportion is small because the more convective regions were avoided to ensure the safety of the aircraft crew. The rest of the data were collected either in stratiform areas (72.6%) or in clear sky (13.1%).

Therefore, the data collected by RASTA during the SOP1 offer a wide variety of conditions (stratiform, convective and clear sky) over land, sea and mountainous regions.

2.3. The Arome-WMed NWP model

Arome-WMed (Fourrié *et al.* 2015) is a configuration of the numerical weather prediction system Arome (Seity *et al.* 2011) that was specially designed for the SOP1. Arome-WMed, which covers the entire northwestern Mediterranean Basin, ran in real time during the SOP1 to plan the airborne operations in advance, especially in the mesoscale convective systems. Here we used the first reanalysis of the SOP1 with Arome-WMed, which assimilates more observations than the real-time version. The first reanalysis fields of Arome-WMed are available from the HyMeX database (doi:10.6096/HYMEX.REANALYSIS_AROME_WMED_V1.2014.02.10). The Arome-WMed domain is displayed in Figure 1.

Arome-WMed ran at a horizontal resolution of 2.5 km $\times$ 2.5 km with 60 vertical levels ranging from approximately 10 m above ground level to 1 hPa. In the model, the deep convection is explicitly resolved and the microphysical processes are governed by the ICE3 one-moment bulk microphysical scheme (Pinty and Jabouille 1998). Six water species are predicted by Arome-WMed (water vapour, rain, cloud liquid droplets, snow, pristine ice and graupel). For each hydrometeor species j, the Particle Size Distributions (PSDs) are expressed as generalized gamma distributions multiplied by their total number concentrations N_{0j}. The PSDs depend on the maximum particle diameters (expressed in metres) and on the hydrometeor contents M_j (expressed in kg.m^{-3}). The general expression is given by

$$N_j(D) = N_{0_j} \frac{\alpha_j}{\Gamma(\nu_j)} \lambda_j^{\alpha_j \nu_j} D^{\alpha_j \nu_j - 1} \exp(-(\lambda_j D)^{\alpha_j}), \qquad (1)$$

where

$$\lambda_j = \left(\frac{M_j \Gamma(\nu_j)}{a_j C_j \Gamma\left(\nu_j + \frac{b_j}{\alpha_j}\right)} \right)^{\frac{1}{X_j - b_j}} \quad , N_{0_j} = C_j \lambda_j^{X_j}.$$

The parameters α_j and ν_j define the shape parameters of the PSDs. The densities are calculated according to the mass–diameter relationship $m_j(D) = a_j D^{b_j}$. The coefficients of the PSDs and the mass–diameter relationships are given in Table 1.

As shown in Table 1, the cloud liquid droplet concentration is three times higher over land than over sea ($3 \cdot 10^8 \mathrm{m}^{-3}$ versus $1 \cdot 10^8 \mathrm{m}^{-3}$). Indeed, cloud droplet concentration increases with aerosol number concentration and, therefore, is higher over land than over sea (Squires 1958; Gultepe and Isaac 2004). For snow, graupel and rain, the PSDs are reduced to exponential distributions.

The Arome-WMed initial conditions are provided by the 00 UTC analysis. The three-dimensional variational (3DVar) data

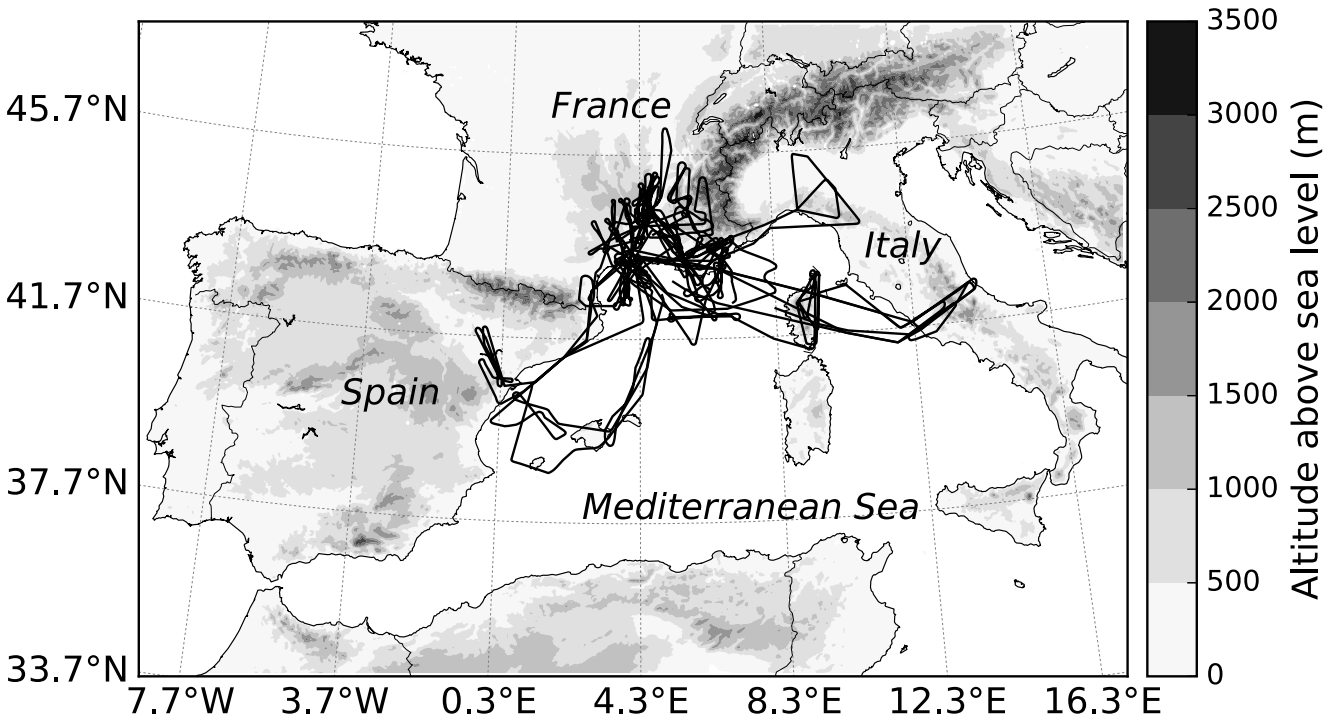

Figure 1. The Falcon 20 flight paths (black lines) during the HyMeX first Special Observing Period over the Arome-WMed domain. The altitude above sea level (in metres) is represented by the colour shades.

Table 1. Coefficients of Particle Size Distributions and mass–diameter relationships as defined in ICE3 for snow, graupel, cloud liquid water, cloud pristine ice and rain.

Type	α_j	ν_j	C_j $[m^{X_j-3}]$	X_j	a_j $[kg\ m^{-b_j}]$	b_j
rain	1	1	$8 \cdot 10^6$	-1	$\frac{\pi\rho_w}{6}$ = 524	3
pristine ice	3	3	C (diagnosed)	0	0.82	2.5
graupel (wet and dry)	1	1	$5 \cdot 10^5$	-0.5	19.6	2.8
snow	1	1	5	1	0.02	1.9
cloud liquid droplet over land	1	3	$3 \cdot 10^8$	0	524	3
cloud liquid droplet over sea	3	1	$1 \cdot 10^8$	0	524	3

assimilation system of Arome-WMed (Brousseau *et al.* 2014) ingests observations from a wide variety of instruments every 3 hours (e.g. satellite, GPS, reflectivity and radial velocity from Doppler ground-based radars of the French network ARAMIS and radiosonde).

The work performed here is the first step towards the assimilation of RASTA data into the Arome model. Therefore, only the 3-hour forecasts starting at 00 UTC, 03 UTC, etc., are compared with the RASTA observations because they will be used as the background for the analysis. Accordingly, the time lag between the model forecasts and observations will be less than $\pm$ 1.5 hours. This is a good compromise between the analysis, which contains uncertainties in the hydrometeors, and a longer forecast, for which errors could become too large. Indeed, because the hydrometeors are not included in the control variable, they are gradually modified and are considered updated once the spin-up time is completed ($\approx$ 1 hour).

3. Description of the forward operator

The cloud radar forward operator described here can be used for airborne and ground-based radars operating in the W-band. It is suitable for a vertically pointing antenna but is adaptable to any other pointing angle. The forward operator was designed for a kilometre-scale NWP model with a bulk microphysical scheme. Its input parameters are temperature, pressure, relative humidity and the hydrometeor contents of the five hydrometeor species (rain, snow, graupel, cloud liquid water and pristine ice) predicted by the model. It returns the simulated reflectivity for the nadir- and zenith-pointing antennas at each range gate. The attenuation is also simulated.

3.1. *Radar equation*

For each of the five types of hydrometeor j of particle size distribution N_j, the reflectivity (in mm^6 m^{-3}) is computed by integrating the backscattering cross section $\sigma_j(D)$ (in m^2) over all the particle diameters D (in metres). At each gate at a distance R (in metres) from the plane, the total reflectivity is then obtained after summing over all types of hydrometeors (rain, pristine ice, snow, graupel and cloud liquid water). The reflectivity, expressed in logarithmic scale (dBZ) because the dynamic of the signal is very large, is given by

$$Z(R) = 10\log_{10}\left(10^{18}\frac{\lambda^4}{\pi^5|K_w|^2}l(R)\sum_{j=1}^{5}\int_{D_{\min}}^{D_{\max}}\sigma_j(D)N_j(D,M_j(R))dD\right), \quad (2)$$

where λ (in metres) is the radar wavelength (3.15 mm for the cloud radar RASTA), M_j is the hydrometeor content (in kg m^{-3}), $|K_w|^2$ is the dielectric factor of the liquid water, which equals 0.75 at 95 GHz at 10° C, and $l(R)$ is the total two-way attenuation computed along the path from the plane altitude h_{RASTA} to the range gate.

The attenuation is obtained according to

$$l(R) = \exp\left(-2\int_{h_{\text{RASTA}}}^{R}\sum_{j=1}^{5}\int_{D_{\min}}^{D_{\max}}C_{ej}(D)N_j(D,M_j(R))dDdR\right), \quad (3)$$

where $C_{ej}(D)$ is the extinction coefficient. Here, the multiplying factor 2 accounts for the two-way paths. Attenuation by moist air and hydrometeors is accounted for.

Attenuation by moist air can be important at the frequency considered here, especially in the lowest layers of the atmosphere ($\approx$ 1dB km^{-1} below an altitude of 1.5 km). Therefore, the effect on the total attenuation is stronger for a ground-based radar because the attenuation caused by moist air in the lowest layers propagates to the other gates along the two-way path. The Liebe (1985) model is used to compute the attenuation by moist air.

At this frequency, even if the reflectivity (in Equation 2) due to cloud liquid water is quite low, the effect on the total attenuation (in Equation 3) can be strong (Di Michele *et al.* 2012). In Equation 3, attenuation due to rainfall is very strong and can be of the order of tens of dB in heavy precipitation, completely extinguishing the signal. Conversely, ice particles have a smaller impact on the total attenuation ($<$ 1 dB km^{-1}).

It is assumed that multiple scattering effects are negligible. For spaceborne radar, multiple scattering effects may impact the reflectivity, especially during heavy convective precipitation events (Battaglia *et al.* 2010; Bouniol *et al.* 2008). These effects are less pronounced for airborne radars because their footprints are much smaller than those of spaceborne radars (Battaglia *et al.* 2007). Therefore, multiple scattering effects are not simulated in the cloud radar forward operator. Nonuniform beam filling effects are also not simulated because the model resolution is coarser than the observational resolution.

Radar sensitivity decreases with increasing range from the radar. To ensure consistency with the observations, the minimum detectable reflectivity is also simulated at each range gate.

N_j and M_j are given by the ICE3 microphysical scheme. The single scattering and hydrometeor dielectric properties need to be specified by making some assumptions in addition to the microphysical scheme. The T-matrix method (Mishchenko *et al.* 1996) is used to compute the radar back-scattering cross section, σ_j, and the extinction coefficient, Ce_j.

3.2. *Single scattering properties*

Raindrops tend to have an oblate spheroidal shape when they fall through the atmosphere. This shape is defined by the ratio of the maximum diameter along the vertical axis to the maximum diameter along the horizontal axis. Augros *et al.* (2016) conducted a sensitivity study for a ground-based precipitation radar forward operator using the same ICE3 microphysical scheme over the SOP1. They found that the formulation from Brandes *et al.* (2002) was best suited to model the raindrop shape. Therefore, this formulation is used in our cloud radar forward operator. The axis ratio r depends on the equivalent-volume drop diameter D_{eq} (in mm) and is forced to 1 for diameters smaller than 0.5 mm. This formulation is given by

$$r = 0.9951 + 0.02510D_{eq} - 0.03644D_{eq}^2 + 0.005303D_{eq}^3 - 0.0002492D_{eq}^4. \quad (4)$$

The cloud liquid water particles can be considered to be spherical, and Mie theory can be used to compute the single scattering properties. Indeed, for a water content of 1 g m^{-3}, the diameter is less than 0.1 mm, which is more than 10 times smaller than the wavelength (3.15 mm). Therefore, for cloud liquid water, we use the T-matrix method with axis ratio equal to 1, which is equivalent to using the Mie theory.

The T-matrix method can also be used for snow, graupel and pristine ice. Ice crystals exhibit many different complex shapes in nature (Korolev *et al.* 2000), and these differences depend on their past evolution and the environment (Bailey and Hallett 2004). Therefore, a large number of scattering methods have been developed to compute their single scattering properties. For example, the Discrete Dipole Approximation (DDA, Draine and Flatau 1994) has been widely used to model specific ice crystal shapes (Hong 2007,Di Michele *et al.* 2012). This method requires high computation memory, especially for large particles. Moreover, the model is unable to predict the particle shapes (e.g. either dendrites, rosettes or columns for crystals), so an assumption has to be made concerning the particle shapes. As in the case of raindrops, an alternative is to use a spheroidal model to define an effective shape and to employ the T-matrix method. As particles fall through the atmosphere, they tend to oscillate around the viewing angle. When the T-matrix method is used, these oscillations are taken into account by using a mean axis ratio, whose value is higher than the real one. Choosing a mean axis ratio instead of modelling the oscillations (ie, specify a canting angle and its distribution) allows the use of a smaller number of free parameters and saves computation time. The effective shape of the particle plays a critical role in computing the backscattering cross section and the extinction coefficient, in particular for nadir/zenith-pointing millimetre-wavelength radars (Hogan *et al.* 2012). Therefore, in Section 4.2, a variational method is applied to retrieve the optimal axis ratio for the three ice species: snow, graupel and pristine ice.

3.3. Hydrometeor dielectric characteristics

We decided to select the same hydrometeor dielectric characteristics used in the polarimetric forward operator of Augros *et al.* (2016), which was also designed for ICE3 but for ground-based centimetre-wavelength radars. Indeed, to be consistent with Arome, the mass–diameter relationships ($m_j = a_j D^{b_j}$) are taken from the ICE3 bulk one-moment microphysical scheme. The coefficients a_j and b_j are given in Table 1.

For small diameters, the densities of the three ice species (graupel, snow and pristine ice) can exceed that of pure ice (912 g m^{-3}). To avoid this unphysical effect, when their densities exceed that of pure ice, the corresponding axis ratio is set to one and the density is set equal to the value of pure ice. For a spherical shape, this occurs for diameters smaller than 0.1 mm for snow, 3 μm for cloud primary pristine ice and 0.16 μm for graupel. The dielectric constant is calculated using the Debye model for rainwater and cloud liquid water. For pristine ice, snow and dry graupel, the Maxwell–Garnett (MG) formulation is employed with ice inclusions in an air matrix.

In ICE3, graupel is the only ice species that can have a wet growth mode. Therefore, a bright band was modelled when there was wet graupel, following the work of Augros *et al.* (2016). The dielectric function is calculated according to Matrosov (2008) and depends on the fraction of liquid water F_w ($F_w = \frac{M_r}{M_r+M_g}$, where M_r and M_g are the hydrometeor contents of rain and graupel, respectively). The dielectric function is then obtained via a linear combination of the MG rule for inclusions of water in a dry graupel matrix ϵ_{gw} and the MG rule for inclusions of graupel in a water matrix ϵ_{wg}. It must be borne in mind that the melting snow flakes undergo structural changes (ie, shape) during the melting process (Kintea *et al.* 2015; Mitra *et al.* 1990). Therefore, we have less confidence in forward modelling the melting layer than the cold and warm phases.

3.4. T-matrix lookup tables

To save computation time when the T-matrix method is employed, T-matrix lookup tables are used for each species. Because this simulator was developed for vertically pointing radars, the lookup tables are calculated for an elevation angle of 90°(the incident wave is perpendicular to the long axis of the spheroid).

The scattering coefficients depend on the temperature, hydrometeor content and liquid water fraction. Therefore, each table contains the scattering coefficients for a given range of these parameters (see Table 2). Hydrometeor contents vary over an interval from 10^{-7} kg m^{-3} to 10^{-2} kg m^{-3}. To model the bright band, the liquid water fraction only varies for the wet graupel when the temperature is between -10°C and $+10$°C.

An axis ratio equal to 1 is equivalent to using the Mie theory. Therefore, when particles are considered to be spherical, we use the T-matrix method with an axis ratio equal to 1, which is the case for cloud liquid water. In addition, T-matrix lookup tables were calculated for axis ratios ranging from 0.4 to 1 for pristine ice and snow and from 0.5 to 1 for graupel. The T-matrix code does not converge for wet graupel when the axis ratio is smaller than 0.5.

4. Validation of the radar forward operator

The forward operator is now validated using RASTA observations and the 3-hour Arome-WMed forecasts. To take the spatial shifts between the observations and simulations into account when validating the forward operator, a novel neighbourhood validation method, called the MRC method, was conceived. This method is described in Section 4.1. In Section 4.2, a variational method is applied to estimate the effective shapes that best fit the observations for the three ice species (graupel, snow and cloud pristine ice). Further comparisons are then shown in Section 4.3 to assess the vertical consistency of the results.

4.1. The Most Resembling Column (MRC) method

4.1.1. Description of the method

The aim of the MRC method is to help assess the degree of realism of the forward operator and calibrate the properties inside the operator. Traditional verification metrics that compare simulated fields directly at observation points present several challenges (Ebert *et al.* 2013), especially for high-resolution NWP models. Grid-to-grid comparisons require a perfect match between forecasts and observations, which is rarely the case. Such a comparison would result in a bias, whose origin cannot be fully attributed either to a spatial mismatch or to a lack of realism within the forward operator. This section explores how spatial and temporal mismatch issues can be overcome to calibrate and validate the forward operator.

Over the last few years, a large number of spatial verification methods have been designed to take into account spatial and temporal mismatches in the verification of model forecasts (Casati *et al.* 2008; Gilleland *et al.* 2009). For example, neighbourhood methods (Roberts and Lean 2008; Amodei *et al.* 2015) can be used to assess the skill of high-resolution models in predicting clouds or precipitation occurring in a given spatial neighbourhood. Other approaches, such as object-based methods (Davis *et al.* 2006), are well suited to study how capable a model is of capturing overall structures. However, these verification methods are two-dimensional and a three-dimensional (3D) method is required here because the synthetic observations are simulated in vertical columns.

Other methods can be used to verify 3D forecast fields. Typically, simulations and observations can be compared via their Contoured Frequency by Altitude Diagram (CFAD, Yuter and Houze 1995) within a given area (see for example Iguchi *et al.* 2012). CFADs represent the distribution of the reflectivity as a function of the altitude. This is an effective way to obtain a statistical view of how the ‘model + forward operator’ can capture cloud vertical structures. If a full 3D structure is observed in a sufficiently large area, the mismatched structures are more likely to be captured by the model and expressed in the CFAD. However, vertical cloud information is only available along the flight track for the cloud radar RASTA. Therefore, some structures can be missed in the RASTA observation dataset even though they are simulated by the model. The Method for Object-Based Diagnostic Evaluation (MODE, Davis *et al.* 2006), recently adapted for a 3D geometry by Miller *et al.* (2014), also requires a full 3D description of distinct cloud objects in both the observations and the simulations, which is not the case with the airborne cloud radar RASTA.

In our case, each observed vertical profile along the aircraft track should ideally be compared with the most resembling vertical column simulated in the forecast field. None of the 3D validation methods listed above are suitable for that purpose.

Table 2. Minimum, step and maximum values for the diameter D, temperature T and fraction liquid water F_w used to compute the T-matrix lookup tables for each hydrometeor species.

Type	D [mm]	T [°]	F_w [%]
rain	0.1;0.5;8	-20;1;40	100
cloud liquid water	0.005;0.01;1.5	-30;1;40	100
pristine ice	0.01;0.01;7.0	-70;1;10	0
dry graupel	0.05;0.15;10.0	-70;1;10	0
wet graupel	0.1;0.2;9.5	-10;1;10	0;10;100
snow	0.1;0.05;20	-70;10;1	0

The neighbourhood validation technique developed here is derived from the one-dimensional (1D) Bayesian retrieval method employed in the first step of the 1D+3DVar assimilation process used to assimilate radar reflectivity in the Arome model (Caumont *et al.* 2010; Wattrelot *et al.* 2014). The methodology behind the MRC method is also similar to the Barker *et al.* (2011) construction algorithm, in which a 3D cloud scene is constructed from passive satellite imagery and collocated 2D vertical profiles of cloud properties. For each observed vertical profile, model-equivalent vertical profiles are simulated within a given neighbourhood around the observed location. The attenuation is computed by positioning the aircraft at its altitude in all considered vertical profiles. The simulated column for which the standard deviation between the observations and simulations is minimal is selected to validate and calibrate the forward operator. Minimising the standard deviation instead of minimising the Root Mean Square Error (RMSE), which was used in the 1D Bayesian retrieval of Caumont *et al.* (2010) and the 3D cloud-construction algorithm of Barker *et al.* (2011), allows circumventing part of the model and observation biases.

An illustration of the MRC method is given in Figure 2 for a portion of the flight of 29 September 2012. For each observed vertical profile along the Falcon 20 track, the most resembling simulated vertical profile is chosen in a 160-km-wide square centred on each observation location. Vertical profiles are shown for every four observation time-steps. The top panel shows the observations, the middle panel shows the co-located simulations and the retrieved vertical profiles are shown in the bottom panel. The aircraft's altitude above sea level is indicated by the black line. The single scattering properties are computed using the T-matrix method and assuming all ice species and cloud liquid water spherical (ie, axis ratio $r = 1$). For raindrops, the axis ratio defined in subsection 3.2 is used.

Figure 2 highlights the benefit of using the MRC neighbourhood method described above. Structures are much closer to the observations in the retrieved profiles than in the co-located ones. For example, at 13 UTC, while there are neither clouds nor precipitation below an altitude of 6 km, the co-located simulated profiles exhibit cloud structures at those levels. These structures are no longer present in the retrieved profiles (bottom panel) at approximately 13 UTC. Meanwhile, at 13:25 UTC, the MRC method allows for the retrieval of the cloud structures that are missing in the co-located profiles.

Therefore, using the MRC method, spatial mismatches can be overcome. Each observed vertical profile is compared with the most resembling simulated vertical profile in a given neighbourhood. There is only one parameter that needs to be set in this method: the size of the neighbourhood area used when searching for the most resembling simulated vertical profile. This is addressed in the next section.

4.1.2. Neighbourhood simulation domain size

For the sake of simplicity, the neighbourhood simulation domain is defined by a square centred on the observation point. Because the computation time increases with the size of the simulation domain, it is time-expensive to have domain sizes that are too large. Another reason for not having too large a domain is that the profiles will become less representative further away, as the meteorological environment can change over $\approx$ 100 km scale. A sensitivity study was performed to determine the optimal domain size for the entire period of the study.

The validation process was performed for all flights for neighbourhoods ranging from 0 km (i.e. co-located with the

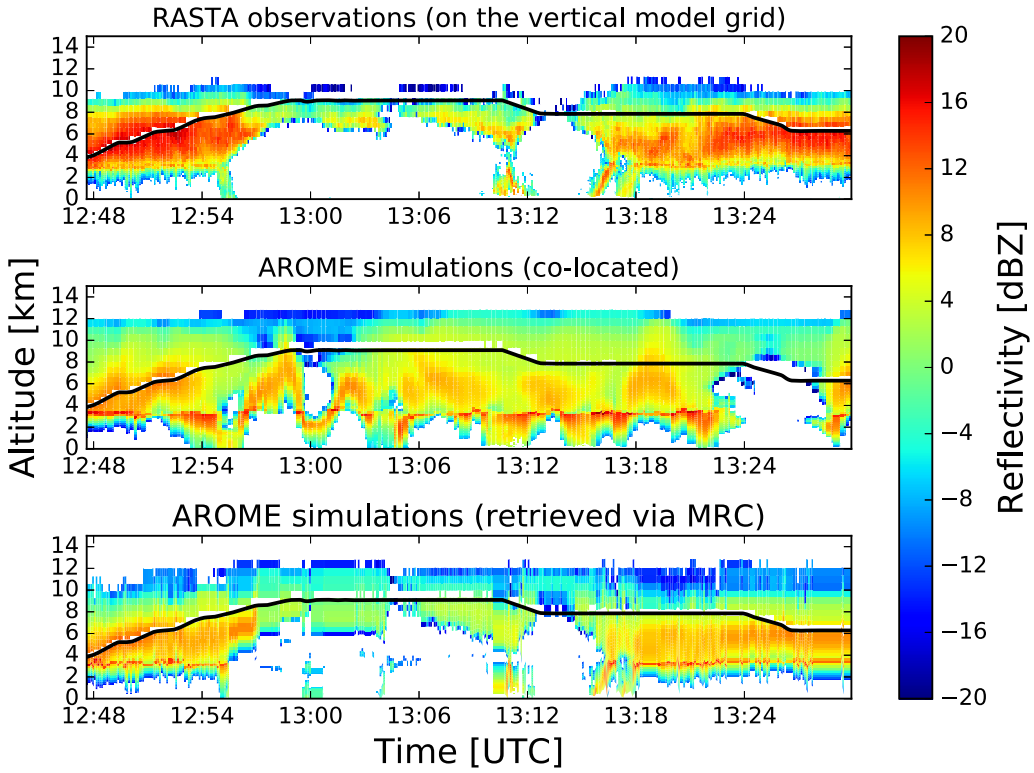

Figure 2. Observed vertical profiles along the aircraft track (top panel) during Flight 17 on 29 September 2012. The corresponding co-located simulated profiles are in the middle panel, and the retrieved simulated profiles are in the bottom panel. Time is on the x-axis and altitude is on the y-axis. The aircraft's altitude above sea level is indicated by the black line.

aircraft) to 160 km (i.e. a 320-km-wide square). This process is repeated for all the observed vertical profiles available during the 3-hour time window centred on the forecast time. The comparison was done as follows. RASTA reflectivities are discarded between 250 m below and 250 m above the aircraft, which corresponds to the minimal measuring range of the nadir- and zenith-pointing antennas. The vertical resolution of the model is coarser than the vertical resolution of RASTA (60 versus 500 vertical levels). Therefore, at each altitude level, the closest observation point (in altitude) is taken for the comparison, so that the RASTA observations match the vertical model grid.

Figure 3 shows the standard deviation between the observed and retrieved vertical profiles as a function of the simulation domain size. The bootstrap confidence intervals were calculated using the Bias-Corrected Accelerated Non-Parametric method (BCa, see Efron *et al.* (1993) 14.3). This method requires a set of independent data. Therefore, vertical profiles were only sampled every 30 observation time-steps for all flights (≈ every 9 km). The results show that the standard deviation decreases exponentially with the neighbourhood size. In addition, the error bars get smaller when the domain size increases. The standard deviation decreases rapidly between 0 km and 150 km and then starts to tend towards a limit value (≈ 2 dB). With a 160-km-wide square, the standard deviation is reduced to less than 5% of its maximum value (≈ 8.45 dB). In addition, the error bars remain approximately constant when the width of the square is larger than 160 km. This size is also also reasonable compared to typical scales of mesoscale variability. Therefore, we decided to use a 160-km-wide square centred on each observation location for the rest of the study.

4.2. Fitting modelled ice hydrometeor axis ratios to measurements

In Figure 2, the reflectivity appears to be underestimated by an order of 10 dB in the ice levels (above ≈ 3.5 km). Such a bias has also been seen in other studies (Hogan *et al.* 2012,Tyynela *et al.* 2011) at the same frequency when Mie theory was used. Therefore, it has been suggested that sphericity may not be a valid approximation to compute single scattering properties for vertically pointing radars.

As explained in Section 3.2, the three ice species can be modelled as oblate spheroids, each of them having their own axis

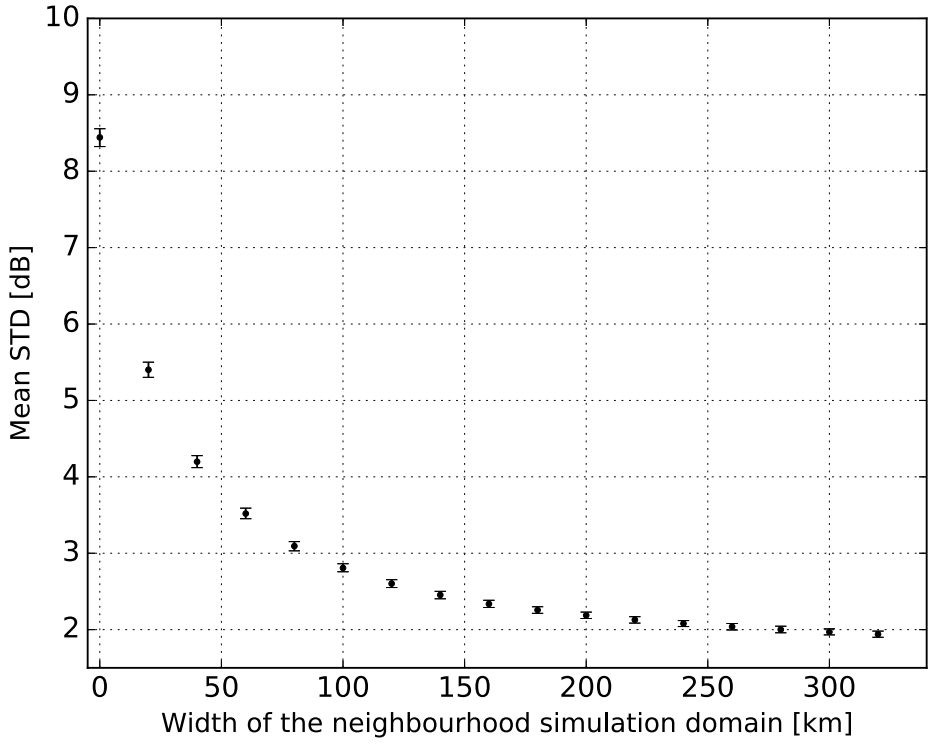

Figure 3. Mean standard deviation (dB) between the observed and retrieved vertical profiles as a function of the width of the neighbourhood simulation domain (in km) for all flights during the SOP1. The error bars represent the 90% bias-corrected and accelerated (BCa) bootstrap confidence intervals (see Efron *et al.* 1993). (There are a total of 3145 vertical columns.)

ratio. The aim of this section is to estimate the axis ratios that best fit the observations for graupel, snow and pristine ice. Recall that the raindrop's axis ratio is defined using the Brandes *et al.* (2002) formulation and that cloud liquid droplets are considered to be spherical.

For ice species, many different values of the axis ratio can be found in the literature. Hogan *et al.* (2012) chose an average axis ratio of 0.6 but pointed out that this value may be influenced by the type of cloud and by their past evolution. Korolev and Isaac (2003) studied the distribution of ice particle axis ratios with a set of 10^6 aircraft images collected in midlatitude and polar stratiform clouds. Depending on the temperature, the average aspect ratio of ice particles was found to range from 0.6 to 0.8. This range of values is also consistent with the study of Garrett *et al.* (2015) in which the median measured aspect ratio ranged from 0.6 to 0.85 depending on the extent of riming (e.g. aggregates, moderately rimed and graupel categories). In addition, Matrosov (2015) estimated ice particle axis ratios from Depolarization Ratio measurements over mountains of approximately 0.5 ± 0.2 depending on the mass–diameter relationship. All these studies suggest that choosing a single axis ratio for all ice species would not be appropriate because they are all defined differently in the ICE3 microphysical scheme.

Therefore, we decided to estimate three different axis ratios for pristine ice (r_i), snow (r_s) and graupel (r_g). It is assumed that wet graupel particles have the same axis ratio as dry graupel particles. For each triplet of axis ratios, simulations were performed for all flights during the observing period. To isolate spatial location errors, they were compared to the observations using the MRC method described in Section 4.1 with a 160-km-wide box centred on each observation position along the aircraft track. The optimal triplet of axis ratios was then retrieved by minimising the standard deviation between observations and simulations. For each combination of axis ratios, the standard deviation between all observed and simulated vertical columns was calculated. The standard deviation reaches its minimum for an optimum triplet of axis ratios of:

- Graupel axis ratio $r_g = 0.8$;
- Snow axis ratio $r_s = 0.7$;
- Pristine ice axis ratio $r_i = 1$.

In addition, Figure 4 shows the standard deviation (on the y-axis) between observations and simulations as a function of one

the three ice species axis ratios (snow axis ratio r_s in Figure 4a, graupel axis ratio r_g in Figure 4b and pristine ice axis ratio r_i in Figure 4c) when the corresponding two other ice species axis ratios are fixed to a given value. Snow axis ratio r_s is the free variable (on the x-axis) in Figure 4a, graupel axis ratio rg is the free variable in Figure 4b and pristine ice axis ratio r_i is the free variable in Figure 4c. For these three Figures, data points are in blue when the corresponding two other ice species are optimum the axis ratios of, in red when they equal to 1 and in green when they are low. The bootstrap confidence interval is also shown for each standard deviation.

These figures demonstrate the sensitivity of the simulations to the combination of the r_g, r_s and r_i properties. Indeed, regardless of the value of the snow axis ratio (r_s) in Figure 4a, if the pristine ice and graupel are considered flattened ($r_g = 0.5$ and $r_i = 0.4$, green data points), the standard deviation is much larger than when they are considered to be either spherical (red data points) or with their optimal axis ratio values ($r_g = 0.8$ and $r_i = 1$, blue data points). The same conclusion can be drawn from Figures 4b and 4c where the variation is shown as a function of the graupel (r_g) and pristine ice (r_i) axis ratios, respectively. Therefore, even if the reflectivity is underestimated with the spherical assumption, this approximation is still more appropriate than using axis ratios that are too low.

When pristine ice and graupel are considered spherical (red data points in Figure 4a), above (below) a snow axis ratio r_s of 0.6, the reflectivity is underestimated (overestimated), which explains why the standard deviation increases when the snow axis ratio deviates from this value of r_s. Even though it is slightly less pronounced when the graupel and pristine ice optimal axis ratio values are used ($r_g = 0.8$ and $r_i = 1$, blue data points), a minimum standard deviation is also obtained for a snow axis ratio r_s equal to 0.7.

The same behaviour is seen in Figure 4b where the variation is shown as a function of the graupel axis ratio (r_g). An optimal value of r_g is reached and the effect is more pronounced when the snow and pristine ice are considered to be spherical (red data points). In addition, when both axis ratios are optimal ($r_s = 0.8$ and $r_i = 1$, blue data points), the standard deviation is minimal for a graupel axis ratio equal to 0.8.

By contrast, Figure 4c indicates that the optimal value for the pristine ice axis ratio r_i is near 1. Indeed, regardless of the values of the graupel and snow axis ratios, the standard deviation decreases with increasing pristine ice axis ratio. This result was unexpected because pristine ice exhibits many different shapes in nature (Korolev and Isaac 2003), such as rosettes or plate-like shapes (Liu 2008), for which the mean axis ratio is expected to be smaller. To quantify the relative contributions of the three ice species to the minimisation, Figure 5 presents the mean vertical profiles of snow (snowflake markers), graupel (circle markers) and pristine ice (square markers) reflectivity over the columns which have been retrieved via the MRC method when ice particles are considered spheroidal with their optimal axis ratio values. Figure 5 shows that graupel is the ice species that mostly contributes to the minimisation between altitudes of 3 km to 5-6 km. Above an altitude of 6 km, the minimisation is mainly dominated by snow. Pristine ice only starts to dominate over snow above an altitude of about 9 km. Therefore, pristine ice is only likely to dominate the radar signal in the upper parts of the clouds, where the reflectivity is overestimated (see Figure 2 for instance), probably because the microphysical scheme ICE3 produces too much pristine ice. So the optimal pristine ice axis ratio is probably overestimated ($r_i = 1$ for a spherical particle) so as to give a lower reflectivity in the upper parts of the clouds.

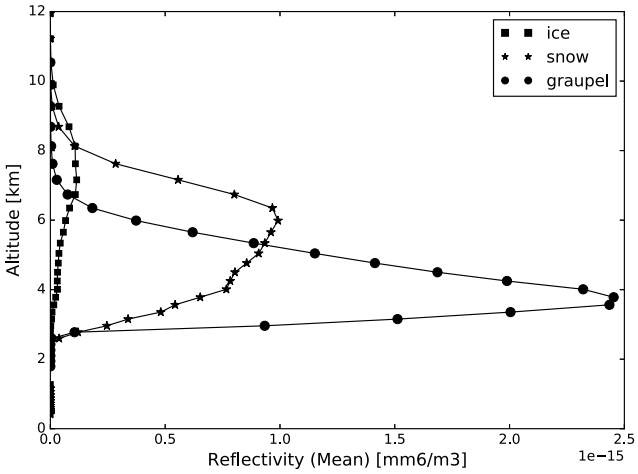

Figure 5. Mean vertical profiles of snow, graupel and pristine ice reflectivity (in $mm^6.m^{-3}$) over all the vertical columns which have been retrieved via the MRC method when when ice particles are considered spheroidal with their optimal values of axis ratios ($rg = 0.8, rs = 0.7, ri = 1$). Snow is represented by the snowflakes, graupel by the circles and pristine ice by the squares.)

The bootstrap confidence intervals in Figures 4a, 4b and 4c are sometimes as large as the difference between the standard

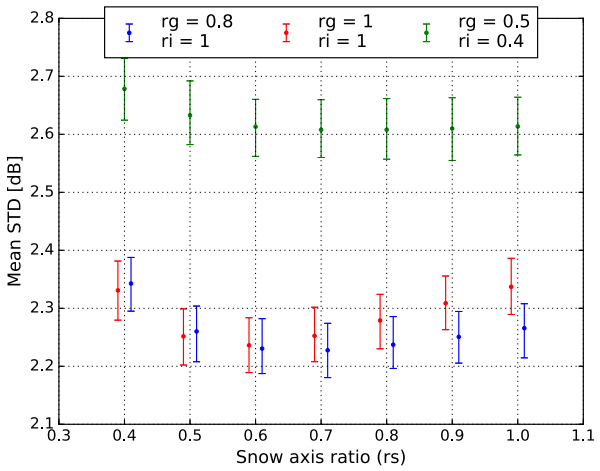

(a)

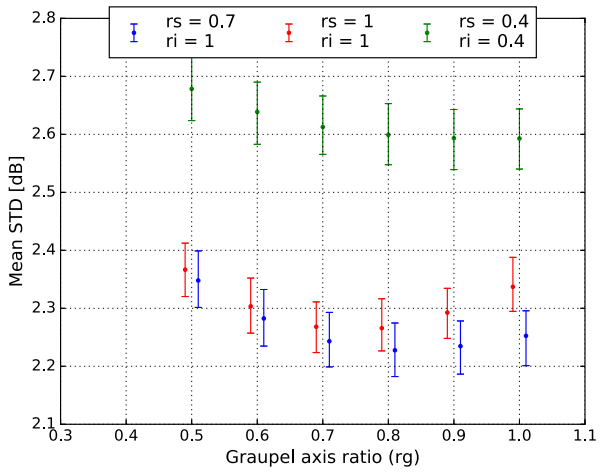

(b)

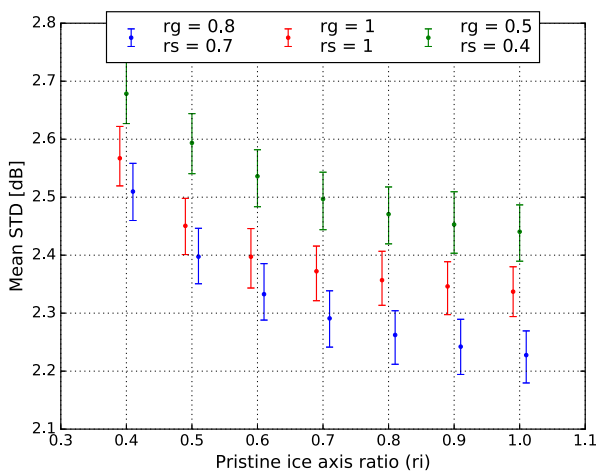

(c)

Figure 4. Mean standard deviation (on the y-axis) between observations and simulations as a function of one the three ice species axis ratios (r_s in Figure 4a, r_g in Figure 4b and r_i in Figure 4c) when the corresponding two other ice species axis ratios are fixed to a given value. Snow axis ratio r_s is the free variable (on the x-axis) in Figure 4a, graupel is the free variable in Figure 4b and pristine ice is the free variable in Figure 4c. For these three Figures, data points are in blue when the corresponding two other ice species are optimum the axis ratios of, in red when they equal to 1 and in green when they are low. The error bars represent the 90% bias-corrected and accelerated (BCa) bootstrap confidence intervals (see Efron *et al.* 1993).

deviations for two different successive evaluated axis ratios. These large values can be attributed to the wide variety of data collected by RASTA over all the flights. Applying the method to only one flight can lead to a different triplet of axis ratios. For example, for the IOP6 flight (24 October 2012), the optimum triplet of axis ratios was 0.8 for graupel, 0.6 for snow and 1 for pristine ice. In this specific case, the observed reflectivity exceeded 10 dBZ in a vertical layer more than 5-km wide with a model snow content of up to 0.6 g m^{-3}. The lower optimum snow axis ratio obtained in this case can be explained by the largest particles that, therefore, have lower axis ratios (Hogan *et al.* 2012). To represent this property, a dependence on the reflectivity value or the hydrometeor content could be taken into account to determine the optimum axis ratios. However, the retrieval would become much more complex because a total of at least six free parameters would have to be estimated (one axis ratio plus one dependency for each ice species).

In this study, the retrieved axis ratios for snow and graupel are slightly higher than those usually reported. Indeed, Fontaine *et al.* (2014) found a mean value of approximately 0.6 and the interval of values reported by Matrosov (2015) was approximately 0.5 ± 0.2 depending on the mass–diameter relationship. The axis ratios used by Putnam *et al.* (2017) are closer to our values (0.75 for snow and graupel); however, they model the oscillations of the particles around the viewing angle. In our study, the oscillations are not modelled; however, they are implicitly taken into account via mean axis ratio values that are higher than the real ones.

On average, using the retrieved optimum triplet of axis ratios enhances the simulated reflectivity. This is demonstrated in Figures 6 and 7 in which time–height cross sections of the reflectivity are shown for RASTA observations (top panel), spherical simulations (middle panel) and spheroidal simulations (bottom panel) using the optimal values of the axis ratios. The IOP6 flight (9 September 2012) is presented in Figure 6, and the IOP16 flight (26 October 2012) is presented in Figure 7. In these two cases, the vertical profiles of the reflectivity are closer to the observations when snow and graupel are simulated as oblate spheroids when their effective axis ratios are optimum (bottom panel). Similar results are obtained for all flights during the observing period; for all cases, it is found that there is much better agreement between the observations and simulations when the optimum effective axis ratios are chosen in the forward operator to compute the single scattering properties.

4.3. Model–Observation comparison

In this section, vertical profiles of the reflectivity simulated with the optimum triplet of axis ratios are compared with those of the observations. To take into account spatial location errors, the MRC method is used and observations are compared to the most resembling simulated column found within a 160-km-wide box centred on each observation location.

4.3.1. Contoured Frequency by Altitude Diagram (CFAD)

Contoured Frequency by Altitude Diagrams (CFADs, Yuter and Houze 1995) are shown for the observations (Figure 8a) and for the reflectivity either simulated using the spherical assumption (Figure 8c) or using the optimum triplet of axis ratios (Figure 8b). The CFADs were computed in bins of 1 dBZ for the reflectivity and 500 m for the altitude. The number of points in each reflectivity bin at each altitude level is represented by colour shades.

For each observed vertical profile, the most resembling column is not necessarily the same when the MRC method is applied to the spheroidal simulations or to the spherical simulations. In all cases, the best profiles (i.e. the most resembling profiles) are selected.

In general, the CFADs indicate that the model and observation distributions have similar structures. Indeed, below an altitude of approximately 3 km, most of the reflectivity lies between -10 dBZ and 10 dBZ in both the observations (Figure 8a) and the simulations (Figures 8b and 8c). Above the bright band ($\sim$ 3.5 km), the reflectivity is primarily distributed near 10 dBZ in the observations, near 8 dBZ in the simulations when all ice species are considered spherical and near 10 dBZ when their effective axis ratios are optimum. Therefore, even though there is a bias in the upper ice levels, the structures are close to each other in both the observations and the simulations. This good agreement is due to the MRC method, in which each observed vertical profile is compared to the most resembling simulated one within the simulation domain.

The CFADs are closer to the observations when the ice species are modelled with their optimal axis ratio values (Figure 8b) than when they are assumed to be spherical (Figure 8c). First, the distribution of the reflectivity as a function of altitude has a more continuous shape from the liquid water levels (below $\sim$ 3.5 km) to the ice levels (above $\sim$ 3.5 km). Second, with the optimal axis ratio values, most of the data are distributed around a value of 9–10 dBZ in the ice levels (above $\sim$ 3.5 km), which is nearly the same as in the observations. By contrast, with the spherical approximation, the data are mostly distributed around 7–8 dBZ at these levels.

This comparison demonstrates more realistic structures when the optimum triplet of axis ratios is used in the cloud radar forward operator to compute the model-equivalent profiles of the reflectivity. Compared to the observations, the bright band is still overestimated. This can be attributed to the overly simplified assumptions in the modelling of the bright band in the forward operator and in the microphysical scheme.

4.3.2. Mean vertical profiles

Figure 9 shows vertical profiles of the bias (left panel) and the standard deviation (right panel) between the simulations and observations for all flights. Simulations were carried out on all flights every four time-steps ($\sim$ 1.2 km), resulting in a total of 23,539 vertical columns. The curves are depicted in green when the three ice species have small axis ratios ($r_g = 0.5$, $r_s = 0.4$ and $r_i = 0.4$), in red when the three are spherical and in blue when

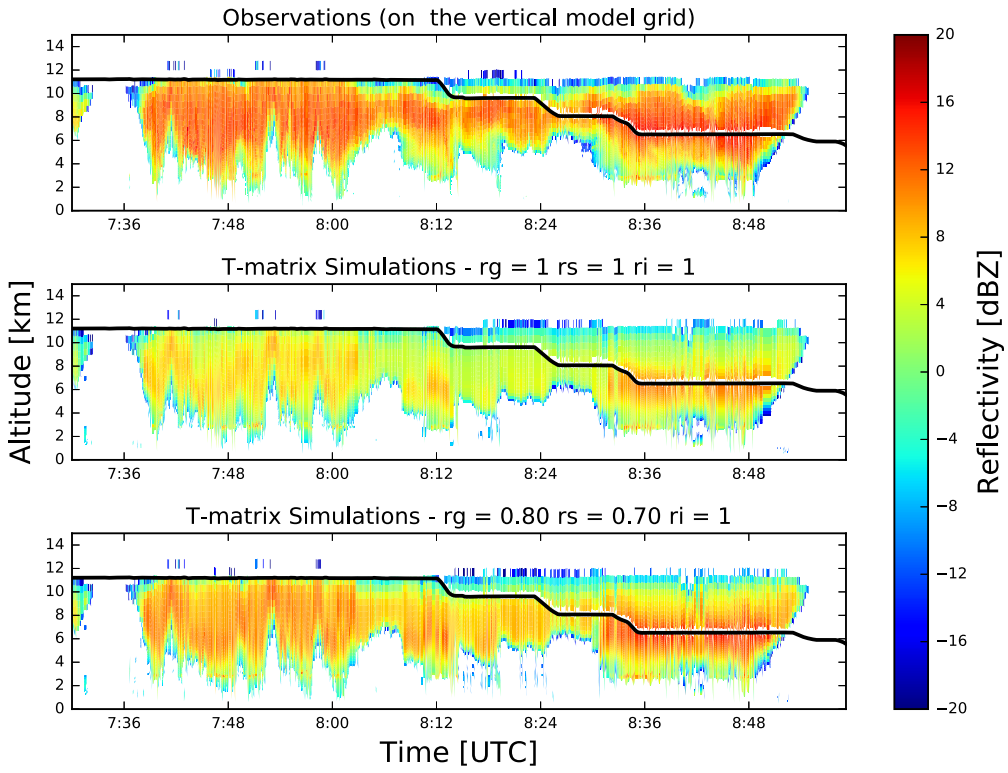

Figure 6. Time–height cross section during IOP6 (24 September 2012). RASTA observations are represented in the top panel, spherical simulations in the middle panel and spheroidal ($r_g = 0.8$, $r_s = 0.7$ and $r_i = 1$) simulations in the bottom panel. Altitude (in km) is on the y-axis and time (in UTC) is on the x-axis. The aircraft's altitude above sea level is represented by the blue line.

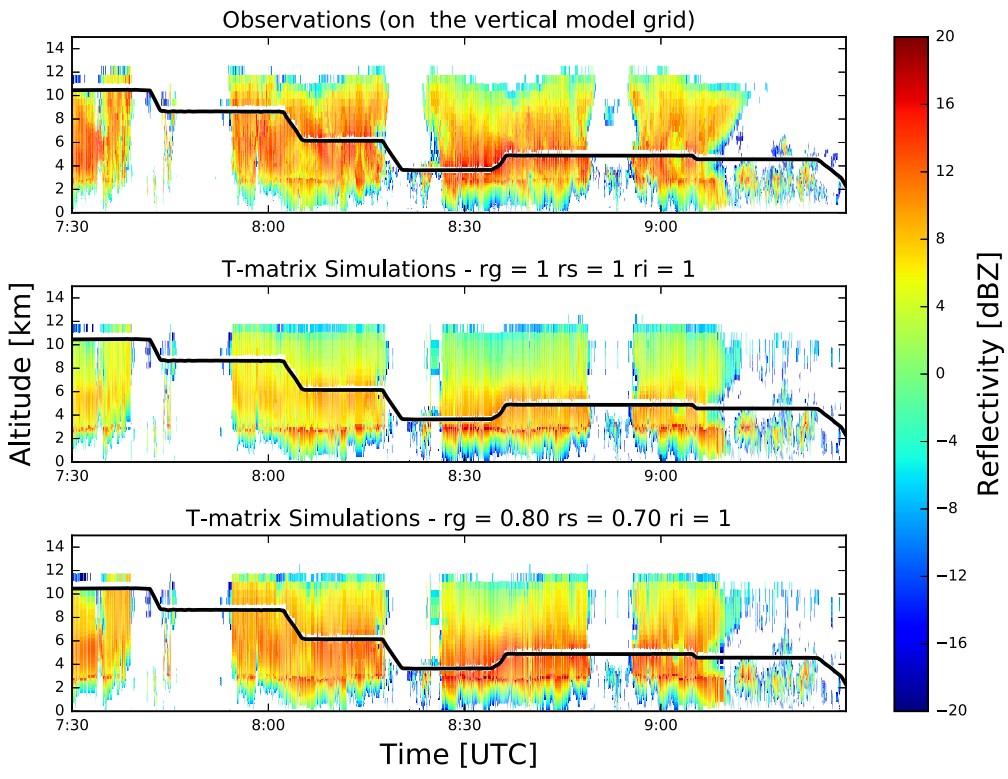

Figure 7. Same as Figure 6 for IOP16 (26 October 2012).

they all have their optimal axis ratio values ($r_g = 0.8$, $r_s = 0.7$ and $r_i = 1$).

The vertical profile of the bias (Figure 9, left panel) exhibits a negative bias when the ice particles are spherical (red curve); this is reduced when the ice particles have smaller axis ratios

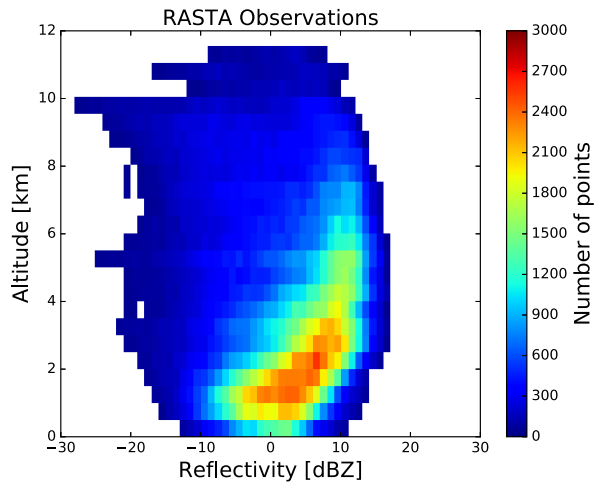

(a)

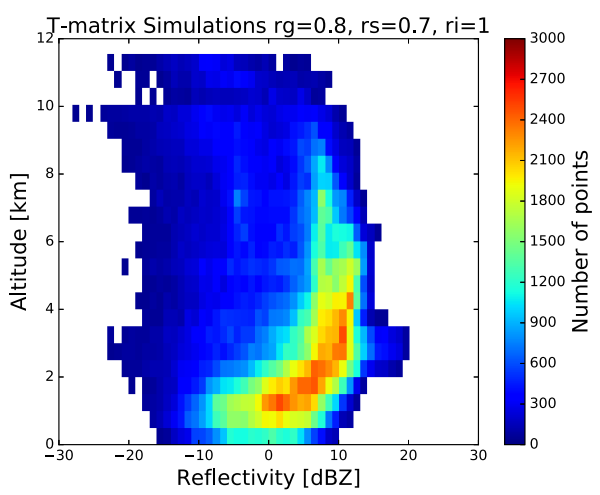

(b)

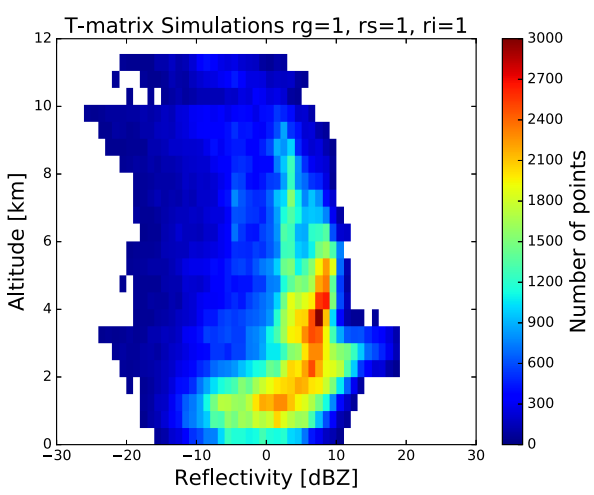

(c)

Figure 8. Cumulated distribution of the (b, c) simulated and (a) observed reflectivity as a function of altitude. Simulations were carried out on all flights every 6 s (a) with the optimal triplet of axis ratios ($r_g = 0.8$, $r_s = 0.7$ and $r_i = 1$) and (b) when ice particles are considered spherical ($r_g = 1$, $r_s = 1$ and $r_i = 1$)

(green and blue curves). This is consistent with the tendency of smaller axis ratios to increase the reflectivity for vertically pointing radars. This underestimation of the mean reflectivity when particles are considered spherical corroborates the previous results for the time–vertical cross sections of the reflectivity (Figure 6 and Figure 7) and the CFADs (Figure 8).

In addition, the vertical profile of the standard deviation (Figure 9, right panel) show that the simulations performed with the optimum triplet of axis ratios are the best at each altitude from 3.5 km to 12 km. Indeed, the standard deviation is quite large for the spherical triplet of axis ratios. The standard deviation decreases when the snow and graupel axis ratios decrease towards their optimum values of 0.7 and 0.8, respectively. Finally, when all axis ratios decrease towards smaller values (green curve), the standard deviation increases again. Below an altitude of approximately 3.5 km, the curves are slightly different even though there are primarily raindrops and cloud liquid droplets at these altitude levels. In all the simulations, raindrops are defined as oblate spheroids, with axis ratios defined in Equation 4 (Brandes *et al*. (2002) formulation), and cloud liquid droplets are considered to be spherical. Therefore, the differences between the curves are attributed to the fact that changes in the ice particle shapes also affect the extinction coefficient in the ice levels and, therefore, the entirety of the vertical profiles of the reflectivity.

In Figure 9 RASTA values at the noise level are also included in the calculation, which explains why we only have a bias of about 1 dB with the spherical simulations.

When the radar reflectivity is only dominated by pristine ice in the upper part of the clouds (above an altitude of $\approx$ 10 km), even though when the smallest pristine ice axis ratio is used (ie, $r_i = 1$) the reflectivity is overestimated. This indicates other biases in the

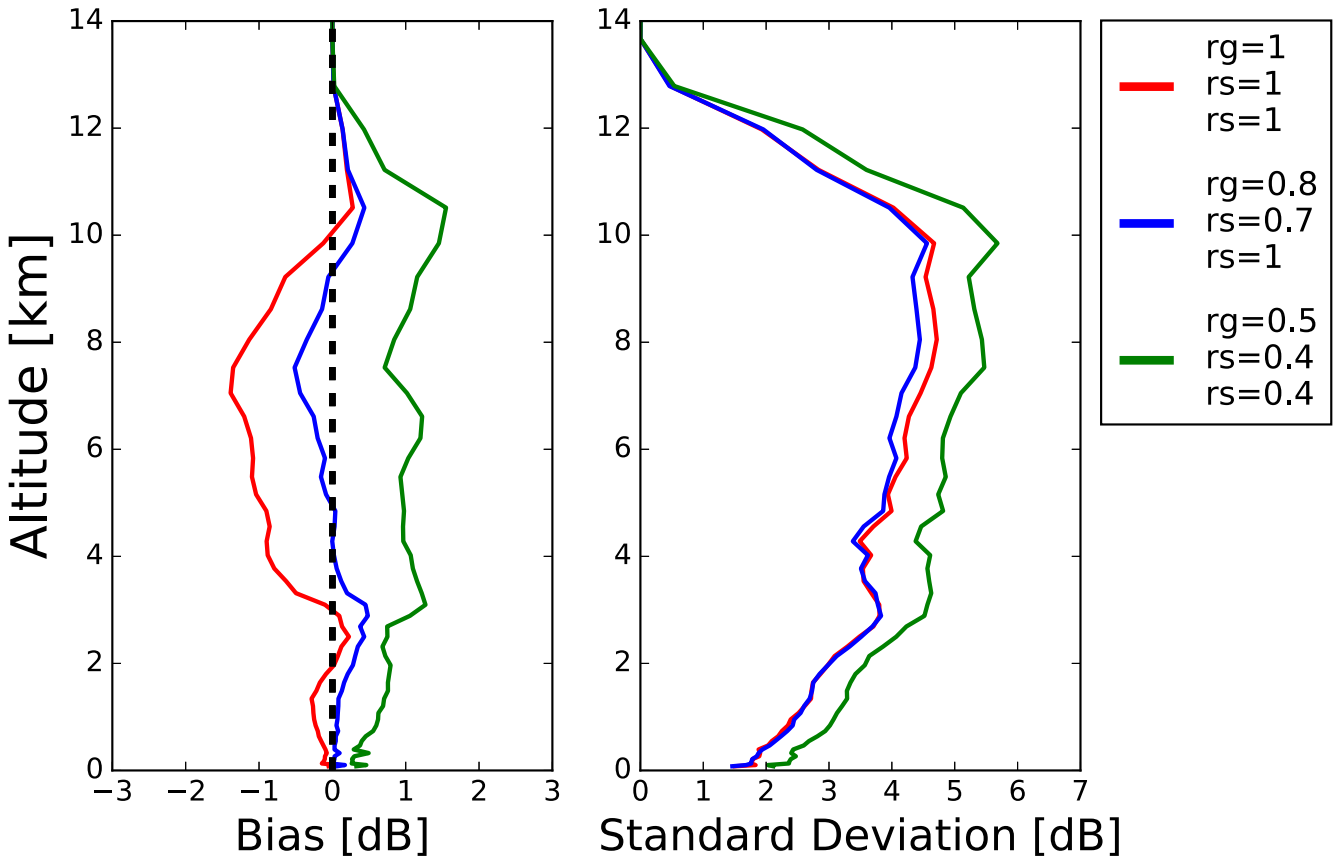

Figure 9. Vertical profiles of the bias and the standard deviation (from left to right) between the simulations and observations for all flights during the observing period ($N = 23,539$). Simulations were carried out with the optimal triplet of axis ratios ($r_g = 0.8$, $r_s = 0.7$ and $r_i = 1$, blue curve), with small axis ratios ($r_g = 0.5$, $r_s = 0.4$ and $r_i = 0.4$, green curve) and with all ice species considered spherical (red curve).

ICE3 microphysical scheme which tends to produce too much pristine ice.

Note that there is a clear benefit of using the triplet of axis ratios that have been retrieved globally by minimising the standard deviation. Indeed, the simulations carried out with the retrieved triplet of axis ratios (Figure 9, blue curve) have a smaller standard deviation at each altitude level than the simulations carried out with either smaller axis ratios (Figure 9, green curve) or a spherical shape (Figure 9, red curve). In addition, there is a reduction in the bias in the ice levels (from 3.5 km to 12 km).

5. Discussion and Conclusions

This paper describes a reflectivity forward operator that was developed for the validation and the assimilation of cloud radar data into Arome-class high-resolution NWP models. It was designed in particular for vertically pointing W-band radars. The forward operator takes as input the hydrometeor contents (rain, cloud liquid droplet, pristine ice, graupel and snow), relative humidity, pressure and temperature. It returns the simulated reflectivity at each range gate from the radar and accounts for hydrometeors and water vapour attenuation.

The forward operator is consistent with the ICE3 one-moment microphysical scheme used in Arome. The T-matrix method is employed to compute the single scattering properties. The effective shape of the particle is either approximated by a sphere or by an oblate spheroid defined by its axis ratio.

The forward operator was validated using data collected in diverse conditions by the airborne cloud radar RASTA during a two-month period over a region of the Mediterranean. To disentangle spatial location errors in the model from errors in the forward operator, a novel neighbourhood validation method, the Most Resembling Column (MRC) method, was designed to validate and calibrate the operator. This method allows us to compare each observed vertical profile with the most resembling simulated profile in a given neighbourhood. A 160-km-wide square simulation domain centred on the observation location was shown to be sufficient to reduce the effects of spatial mismatches. This new method can be used for any forward operator designed

for instruments measuring the vertical distribution of clouds and precipitation (aboard spacecraft or ground-based).

The MRC method was then applied to retrieve the optimal effective shapes (i.e. the mean axis ratios) of the predicted graupel, snow and pristine ice, by minimising the standard deviation between observations and simulations. Even though clouds do not contain a significant quantity of spherical ice particles (Korolev and Isaac 2003), the results indicate that pristine ice can be approximated by a sphere. This discrepancy can be explained by a bias in the ICE3 microphysical scheme which tends to produce too much pristine ice. Therefore, to compensate this bias, the best fit axis ratio is the one which gives the lowest reflectivity (ie, $r_i = 1$ in our case). This spherical retrieval would not necessarily be the same if the amount of pristine ice produced by the microphysical scheme were more realistic. The optimum mean axis ratio is approximately 0.8 for graupel and 0.7 for snow. Simulations carried out with these optimal values were improved for all ice levels (from 3.5 km to 12 km). The spherical approximation leads to an underestimation of the simulated reflectivity by an order of approximately 10 dB. Conversely, if the ice particles are too flattened (i.e. having plate-like shapes), the reflectivity is overestimated. Therefore, the axis ratios should be chosen to be close to their optimal values to obtain good agreement between observations and simulations.

In this study, the retrieved axis ratios were towards the higher end of those reported in prior studies ($\sim$ 0.5–0.8). Contrary to most other studies, in this study the oscillation of the ice particles around the viewing angle is not simulated explicitly. Instead, it is taken into account by using an effective axis ratio, whose value is supposed to be higher than the actual value. Also, one should bear in mind that our confidence intervals are quite large.

Only one axis ratio can be retrieved per ice species. One possibility would be to add a dependence either on the reflectivity or on the hydrometeor content. It could also be interesting to take advantage of the information provided by RASTA Doppler measurements on the hydrometeor fall speed and, therefore, on their sizes. In addition, the RASTA radar will soon be upgraded to provide polarimetric data, which will be of particular interest for characterizing the shapes of hydrometeors.

Prior studies pointed out that spheroids are not an ideal model for snowflakes (Stein *et al.* 2015; Tyynela *et al.* 2011). As an alternative, more complex methods, such as the DDA, can be used to account for non-sphericity (see for example Di Michele *et al.* 2012, Iguchi *et al.* 2012). However, this study shows that treating ice particles as oblate spheroids leads to good agreement between observations and model simulations when the axis ratios are properly specified. The same conclusion as stated by Hogan *et al.* (2012) can be drawn: choosing a mean axis ratio to model an effective shape is an efficient and convenient approximation at this frequency for nadir/zenith-pointing radars.

The reflectivity forward operator developed here can be used as a validation tool, for example to assess the benefits of a two-moment microphysical scheme over a one-moment microphysical scheme. This will be possible in the near future because a new two-moment microphysical scheme (LIMA, see Vié *et al.* 2016) is being implemented in Arome. This forward operator is also the first step towards the assimilation of W-band radar data into kilometre-scale NWP models. Currently, this type of data is not assimilated in these models.

Acknowledgement

This work is a contribution to the HyMeX program supported by MISTRALS, ANR IODA-MED Grant ANR-11-BS56-0005 and ANR MUSIC Grant ANR-14-CE01-0014. This work was supported by the French national programme LEFE/INSU. The authors acknowledge the DGA (Direction Générale de l'Armement), a part of the French Ministry of Defense, for its contribution to Mary Borderies's PhD. The authors are grateful to Christian Chwala for providing the Python implementation of the MPM millimetre wave propagation model. Two anonymous reviewers are also gratefully acknowledged for their comments that helped to significantly improve the quality of the paper.

References

Amodei M, Sanchez I, Stein J. 2015. Verification of the French operational high-resolution model AROME with the regional Brier probability score. *Met. Apps* **22**(4): 731–745, doi:10.1002/met.1510, URL `http://dx.doi.org/10.1002/met.1510`.

Augros C, Caumont O, Ducrocq V, Gaussiat N, Tabary P. 2016. Comparisons between S-, C- and X-band polarimetric radar observations and convective-scale simulations of the HyMeX first special observing period. *Quarterly Journal of the Royal Meteorological Society* **142**: 347–362, doi:10.1002/qj.2572, URL http://dx.doi.org/10.1002/qj.2572.

Bailey M, Hallett J. 2004. Growth rates and habits of ice crystals between -20° and -70°C. *Journal of the Atmospheric Sciences* **61**(5): 514–544, doi:10.1175/1520-0469(2004)061<0514:GRAHOI>2.0.CO;2, URL http://dx.doi.org/10.1175/1520-0469(2004)061<0514:GRAHOI>2.0.CO;2.

Barker H, Jerg M, Wehr T, Kato S, Donovan D, Hogan R. 2011. A 3d cloud-construction algorithm for the earthcare satellite mission. *Quarterly Journal of the Royal Meteorological Society* **137**(657): 1042–1058, doi:10.1002/qj.824.

Battaglia A, Ajewole M, Simmer C. 2007. Evaluation of radar multiple scattering effects in Cloudsat configuration. *Atmospheric Chemistry and Physics* **7**(7): 1719–1730.

Battaglia A, Tanelli S, Kobayashi S, Zrnic D, Hogan RJ, Simmer C. 2010. Multiple-scattering in radar systems: A review. *Journal of Quantitative Spectroscopy and Radiative Transfer* **111**(6): 917–947, doi:10.1016/j.jqsrt.2009.11.024, URL http://dx.doi.org/10.1016/j.jqsrt.2009.11.024.

Bodas-Salcedo A, Webb MJ, Brooks ME, Ringer MA, Williams KD, Milton SF, Wilson DR. 2008. Evaluating cloud systems in the Met Office global forecast model using simulated Cloudsat radar reflectivities. *Journal of Geophysical Research* **113**, doi:10.1029/2007jd009620, URL http://dx.doi.org/10.1029/2007jd009620.

Bouniol D, Protat A, Plana-Fattori A, Giraud M, Vinson JP, Grand N. 2008. Comparison of Airborne and Spaceborne 95-GHz Radar Reflectivities and Evaluation of Multiple Scattering Effects in Spaceborne Measurements. *Journal of Atmospheric and Oceanic Technology* **25**(11): 1983–1995, doi:10.1175/2008jtecha1011.1, URL http://dx.doi.org/10.1175/2008JTECHA1011.1.

Bousquet O, Delanoë J, Bielli S. 2016. Evaluation of 3D wind observations inferred from the analysis of airborne and ground-based radars during HyMeX SOP-1. *Quarterly Journal of the Royal Meteorological Society* .

Brandes EA, Zhang G, Vivekanandan J. 2002. Experiments in Rainfall Estimation with a Polarimetric Radar in a Subtropical Environment. *J. Appl. Meteor.* **41**(6): 674–685, doi:10.1175/1520-0450(2002)041<0674:eirewa>2.0.co;2, URL http://dx.doi.org/10.1175/1520-0450(2002)041<0674:EIREWA>2.0.CO;2.

Brousseau P, Desroziers G, Bouttier F, Chapnik B. 2014. A posterioridiagnostics of the impact of observations on the AROME-France convective-scale data assimilation system. *Quarterly Journal of the Royal Meteorological Society* **140**(680): 982–994, doi:10.1002/qj.2179, URL http://dx.doi.org/10.1002/qj.2179.

Casati B, Wilson LJ, Stephenson DB, Nurmi P, Ghelli A, Pocernich M, Damrath U, Ebert EE, Brown BG, Mason S. 2008. Forecast verification: current status and future directions. *Met. Apps* **15**(1): 3–18, doi:10.1002/met.52, URL http://dx.doi.org/10.1002/met.52.

Caumont O, Ducrocq V, Wattrelot É, Jaubert G, Pradier-Vabre S. 2010. 1D+3DVar assimilation of radar reflectivity data: a proof of concept. *Tellus A* **62**(2): 173–187, doi:10.1111/j.1600-0870.2009.00430.x, URL http://dx.doi.org/10.1111/j.1600-0870.2009.00430.x.

Davis C, Brown B, Bullock R. 2006. Object-Based Verification of Precipitation Forecasts. Part i: Methodology and Application to Mesoscale Rain Areas. *Monthly Weather Review* **134**(7): 1772–1784, doi:10.1175/mwr3145.1, URL http://dx.doi.org/10.1175/MWR3145.1.

Delanoë J, Hogan RJ. 2008. A variational scheme for retrieving ice cloud properties from combined radar, lidar, and infrared radiometer. *Journal of Geophysical Research* **113**(D7), doi:10.1029/2007jd009000, URL http://dx.doi.org/10.1029/2007JD009000.

Delanoë J, Protat A, Jourdan O, Pelon J, Papazzoni M, Dupuy R, Gayet JF, Jouan C. 2013. Comparison of Airborne In Situ, Airborne Radar–Lidar, and Spaceborne Radar–Lidar Retrievals of Polar Ice Cloud Properties Sampled during the POLARCAT Campaign. *Journal of Atmospheric and Oceanic Technology* **30**(1): 57–73, doi:10.1175/JTECH-D-11-00200.1, URL http://dx.doi.org/10.1175/JTECH-D-11-00200.1.

Delanoë J, Protat A, Vinson JP, Brett W, Caudoux C, Bertrand F, Parent du Chatelet J, Hallali R, Barthes L, Haeffelin M, *et al.* 2016. BASTA: A 95-GHz FMCW Doppler Radar for Cloud and Fog Studies. *Journal of Atmospheric and Oceanic Technology* **33**(5): 1023–1038.

Di Michele S, Ahlgrimm M, Forbes R, Kulie M, Bennartz R, Janisková M, Bauer P. 2012. Interpreting an evaluation of the ECMWF global model with Cloudsat observations: ambiguities due to radar reflectivity forward operator uncertainties. *Q.J.R. Meteorol. Soc.* **138**(669): 2047–2065, doi:10.1002/qj.1936, URL http://dx.doi.org/10.1002/qj.1936.

Draine BT, Flatau PJ. 1994. Discrete-Dipole Approximation For Scattering Calculations. *J. Opt. Soc. Am. A* **11**(4): 1491, doi:10.1364/josaa.11.001491, URL http://dx.doi.org/10.1364/JOSAA.11.001491.

Ducrocq V, Braud I, Davolio S, Ferretti R, Flamant C, Jansa A, Kalthoff N, Richard E, Taupier-Letage I, Ayral PA, *et al.* 2014. HyMeX-SOP1: The field campaign dedicated to heavy precipitation and flash flooding in the northwestern Mediterranean. *Bulletin of the American Meteorological Society* **95**(7): 1083–1100.

Ebert E, Wilson L, Weigel A, Mittermaier M, Nurmi P, Gill P, Göber M, Joslyn S, Brown B, Fowler T, Watkins A. 2013. Progress and challenges in forecast verification. *Meteorological Applications* **20**(2): 130–139, doi:10.1002/met.1392, URL https://doi.org/10.1002%2Fmet.1392.

Efron B, Tibshirani RJ, *et al.* 1993. An introduction to the bootstrap.

Fontaine E, Schwarzenboeck A, Delanoë J, Wobrock W, Leroy D, Dupuy R, Gourbeyre C, Protat A. 2014. Constraining mass–diameter relations from hydrometeor images and cloud radar reflectivities in tropical continental

and oceanic convective anvils. *Atmos. Chem. Phys.* **14**(20): 11 367–11 392, doi:10.5194/acp-14-11367-2014, URL http://dx.doi.org/10.5194/acp-14-11367-2014.

Fourrié N, Bresson É, Nuret M, Jany C, Brousseau P, Doerenbecher A, Kreitz M, Nuissier O, Sevault E, Bénichou H, et al. 2015. AROME-WMED, a real-time mesoscale model designed for the HyMeX special observation periods. *Geosci. Model Dev.* **8**(7): 1919–1941, doi:10.5194/gmd-8-1919-2015, URL http://dx.doi.org/10.5194/gmd-8-1919-2015.

Garrett TJ, Yuter SE, Fallgatter C, Shkurko K, Rhodes SR, Endries JL. 2015. Orientations and aspect ratios of falling snow. *Geophysical Research Letters* **42**(11): 4617–4622, doi:10.1002/2015gl064040, URL http://dx.doi.org/10.1002/2015GL064040.

Gilleland E, Ahijevych D, Brown BG, Casati B, Ebert EE. 2009. Intercomparison of Spatial Forecast Verification Methods. *Weather and Forecasting* **24**(5): 1416–1430, doi:10.1175/2009waf2222269.1, URL https://doi.org/10.1175%2F2009waf2222269.1.

Gultepe I, Isaac G. 2004. Aircraft observations of cloud droplet number concentration: Implications for climate studies. *Quarterly Journal of the Royal Meteorological Society* **130**(602): 2377–2390, doi:10.1256/qj.03.120, URL https://doi.org/10.1256%2Fqj.03.120.

Hagen M, Hirsch L, Konow H, Mech FAM, Orlandi E, Crewell S, Groß S, Fix A, Wirth M. 2014. Airborne remote sensing of cloud properties with the german research aircraft HALO.

Haynes J, Marchand R, Luo Z, Bodas-Salcedo A, Stephens G. 2007. A multipurpose radar simulation package: QuickBeam. *Bulletin of the American Meteorological Society* **88**(11): 1723.

Hogan RJ, Tian L, Brown PRA, Westbrook CD, Heymsfield AJ, Eastment JD. 2012. Radar Scattering from Ice Aggregates Using the Horizontally Aligned Oblate Spheroid Approximation. *Journal of Applied Meteorology and Climatology* **51**(3): 655–671, doi:10.1175/jamc-d-11-074.1, URL http://dx.doi.org/10.1175/JAMC-D-11-074.1.

Hong G. 2007. Radar backscattering properties of nonspherical ice crystals at 94 GHz. *Journal of Geophysical Research* **112**(D22), doi:10.1029/2007jd008839, URL http://dx.doi.org/10.1029/2007JD008839.

Horie H, Okamoto H, Iwasaki S, Kumagai H, Kuroiwa H. 2000. Cloud observation with CRL airborne cloud profiling radar (SPIDER). In: *Geoscience and Remote Sensing Symposium, 2000. Proceedings. IGARSS 2000. IEEE 2000 International*, vol. 1. pp. 190–191 vol.1, doi:10.1109/IGARSS.2000.860464.

Iguchi T, Nakajima T, Khain AP, Saito K, Takemura T, Okamoto H, Nishizawa T, Tao WK. 2012. Evaluation of Cloud Microphysics in JMA-NHM Simulations Using Bin or Bulk Microphysical Schemes through Comparison with Cloud Radar Observations. *Journal of the Atmospheric Sciences* **69**(8): 2566–2586, doi:10.1175/jas-d-11-0213.1, URL http://dx.doi.org/10.1175/JAS-D-11-0213.1.

Illingworth AJ, Barker HW, Beljaars A, Ceccaldi M, Chepfer H, Clerbaux N, Cole J, Delanoë J, Domenech C, Donovan DP, et al. 2015. The EarthCARE Satellite: The Next Step Forward in Global Measurements of Clouds, Aerosols, Precipitation, and Radiation. *Bulletin of the American Meteorological Society* **96**(8): 1311–1332, doi:10.1175/bams-d-12-00227.1, URL http://dx.doi.org/10.1175/BAMS-D-12-00227.1.

Kintea DM, Hauk T, Roisman IV, Tropea C. 2015. Shape evolution of a melting nonspherical particle. *Phys. Rev. E* **92**: 033 012, doi:10.1103/PhysRevE.92.033012, URL https://link.aps.org/doi/10.1103/PhysRevE.92.033012.

Kollias P, Clothiaux EE, Miller MA, Albrecht BA, Stephens GL, Ackerman TP. 2007. Millimeter-wavelength radars: New frontier in atmospheric cloud and precipitation research. *Bulletin of the American Meteorological Society* **88**(10): 1608–1624, doi:10.1175/BAMS-88-10-1608, URL http://dx.doi.org/10.1175/BAMS-88-10-1608.

Korolev A, Isaac G. 2003. Roundness and Aspect Ratio of Particles in Ice Clouds. *Journal of the Atmospheric Sciences* **60**(15): 1795–1808, doi:10.1175/1520-0469(2003)060<1795:raarop>2.0.co;2, URL http://dx.doi.org/10.1175/1520-0469(2003)060<1795:RAAROP>2.0.CO;2.

Korolev A, Isaac G, Hallett J. 2000. Ice particle habits in stratiform clouds. *Quarterly Journal of the Royal Meteorological Society* **126**(569): 2873–2902, doi:10.1256/smsqj.56912, URL http://dx.doi.org/10.1256/smsqj.56912.

Leinonen J, Lebsock MD, Tanelli S, Suzuki K, Yashiro H, Miyamoto Y. 2015. Performance assessment of a triple-frequency spaceborne cloud–precipitation radar concept using a global cloud-resolving model. *Atmospheric Measurement Techniques* **8**(8): 3493–3517, doi:10.5194/amt-8-3493-2015, URL http://dx.doi.org/10.5194/amt-8-3493-2015.

Lhermitte R. 1987. A 94 GHz Doppler radar for clouds observations. *J. Atmos. Oceanic Technol* **4**: 36–48.

Li L, Heymsfield GM, Tian L, Racette PE. 2005. Measurements of ocean surface backscattering using an airborne 94-GHz cloud radar-implication for calibration of airborne and spaceborne W-band radars. *Journal of Atmospheric and Oceanic Technology* **22**(7): 1033–1045, doi:10.1175/JTECH1722.1, URL http://dx.doi.org/10.1175/JTECH1722.1.

Li L, Sekelsky SM, Reising SC, Swift CT, Durden SL, Sadowy GA, Dinardo SJ, Li FK, Huffman A, Stephens G, Babb DM, Rosenberger HW. 2001. Retrieval of Atmospheric Attenuation Using Combined Ground-Based and Airborne 95-GHz Cloud Radar Measurements. *Journal of Atmospheric and Oceanic Technology* **18**(8): 1345–1353, doi:10.1175/1520-0426(2001)018<1345:ROAAUC>2.0.CO;2, URL http://dx.doi.org/10.1175/1520-0426(2001)018<1345:ROAAUC>2.0.CO;2.

Liebe HJ. 1985. An updated model for millimeter wave propagation in moist air. *Radio Science* **20**(5): 1069–1089.

Liu G. 2008. A Database of Microwave Single-Scattering Properties for Nonspherical Ice Particles. *Bulletin of the American Meteorological Society* **89**(10): 1563–1570, doi:10.1175/2008bams2486.1, URL http://dx.doi.org/10.1175/2008BAMS2486.1.

Matrosov S. 2008. Assessment of Radar Signal Attenuation Caused by the Melting Hydrometeor Layer. *IEEE Transactions on Geoscience and Remote Sensing* **46**(4): 1039–1047, doi:10.1109/tgrs.2008.915757, URL http://dx.doi.org/10.1109/TGRS.2008.915757.

Matrosov SY. 2015. Evaluations of the Spheroidal Particle Model for Describing Cloud Radar Depolarization Ratios of Ice Hydrometeors. *Journal of Atmospheric and Oceanic Technology* **32**(5): 865–879, doi:10.1175/jtech-d-14-00115.1, URL http://dx.doi.org/10.1175/JTECH-D-14-00115.1.

Miller SD, Weeks CE, Bullock RG, Forsythe JM, Kucera PA, Brown BG, Wolff CA, Partain PT, Jones AS, Johnson DB. 2014. Model-Evaluation Tools for Three-Dimensional Cloud Verification via Spaceborne Active Sensors. *Journal of Applied Meteorology and Climatology* **53**(9): 2181–2195, doi:10.1175/jamc-d-13-0322.1, URL http://dx.doi.org/10.1175/JAMC-D-13-0322.1.

Mishchenko MI, Travis LD, Mackowski DW. 1996. T-matrix computations of light scattering by nonspherical particles: A review. *Journal of Quantitative Spectroscopy and Radiative Transfer* **55**(5): 535–575, doi:10.1016/0022-4073(96)00002-7, URL http://dx.doi.org/10.1016/0022-4073(96)00002-7.

Mitra S, Vohl O, Ahr M, Pruppacher H. 1990. A wind tunnel and theoretical study of the melting behavior of atmospheric ice particles. iv: Experiment and theory for snow flakes. *Journal of the Atmospheric Sciences* **47**(5): 584–591, doi:10.1175/1520-0469(1990)047<0584:awtats>2.0.co;2, URL https://doi.org/10.1175/1520-0469(1990)047<0584:AWTATS>2.0.CO;2.

Mitrescu C, Miller S, Hawkins J, L'Ecuyer T, Turk J, Partain P, Stephens G. 2008. Near-real-time applications of cloudsat data. *Journal of Applied Meteorology and Climatology* **47**(7): 1982–1994, doi:10.1175/2007JAMC1794.1, URL http://dx.doi.org/10.1175/2007JAMC1794.1.

Moran KP, Martner BE, Post MJ, Kropfli RA, Welsh DC, Widener KB. 1998. An Unattended Cloud-Profiling Radar for Use in Climate Research. *Bulletin of the American Meteorological Society* **79**(3): 443–455, doi:10.1175/1520-0477(1998)079<0443:AUCPRF>2.0.CO;2, URL http://dx.doi.org/10.1175/1520-0477(1998)079<0443:AUCPRF>2.0.CO;2.

Pinty J, Jabouille P. 1998. A mixed-phase cloud parameterization for use in mesoscale non-hydrostatic model: simulations of a squall line and of orographic precipitations. In: *Conf. on Cloud Physics*. Amer. Meteor. Soc Everett, WA, pp. 217–220.

Protat A, Bouniol D, Delanoë J, O'Connor E, May P, Plana-Fattori A, Hasson A, Görsdorf U, Heymsfield A. 2009. Assessment of CloudSat reflectivity measurements and ice cloud properties using ground-based and airborne cloud radar observations. *Journal of Atmospheric and Oceanic Technology* **26**(9): 1717–1741, doi:10.1175/2009JTECHA1246.1, URL http://dx.doi.org/10.1175/2009JTECHA1246.1.

Protat A, Delanoë J, Strapp J, Fontaine E, Leroy D, Schwarzenboeck A, Lilie L, Davison C, Dezitter F, Grandin A, *et al.* 2016. The Measured Relationship between Ice Water Content and Cloud Radar Reflectivity in Tropical Convective clouds. *Journal of Applied Meteorology and Climatology* (2016).

Protat A, Young SA, Rikus L, Whimpey M. 2014. Evaluation of hydrometeor frequency of occurrence in a limited-area numerical weather prediction system using near real-time CloudSat-CALIPSO observations. *Q.J.R. Meteorol. Soc.* **140**(685): 2430–2443, doi:10.1002/qj.2308, URL http://dx.doi.org/10.1002/qj.2308.

Putnam BJ, Xue M, Jung Y, Zhang G, Kong F. 2017. Simulation of Polarimetric Radar Variables from 2013 CAPS Spring Experiment Storm-Scale Ensemble Forecasts and Evaluation of Microphysics Schemes. *Monthly Weather Review* **145**(1): 49–73, doi:10.1175/mwr-d-15-0415.1, URL https://doi.org/10.1175%2Fmwr-d-15-0415.1.

Reitter S, Fröhlich K, Seifert A, Crewell S, Mech M. 2011. Evaluation of ice and snow content in the global numerical weather prediction model GMe with CloudSat. *Geosci. Model Dev.* **4**(3): 579–589, doi:10.5194/gmd-4-579-2011, URL http://dx.doi.org/10.5194/gmd-4-579-2011.

Roberts NM, Lean HW. 2008. Scale-Selective Verification of Rainfall Accumulations from High-Resolution Forecasts of Convective Events. *Monthly Weather Review* **136**(1): 78–97, doi:10.1175/2007mwr2123.1, URL http://dx.doi.org/10.1175/2007MWR2123.1.

Seity Y, Brousseau P, Malardel S, Hello G, Bénard P, Bouttier F, Lac C, Masson V. 2011. The AROME-France Convective-Scale Operational Model. *Monthly Weather Review* **139**(3): 976–991, doi:10.1175/2010mwr3425.1, URL http://dx.doi.org/10.1175/2010MWR3425.1.

Squires P. 1958. The Microstructure and Colloidal Stability of Warm Clouds. *Tellus* **10**(2): 256–261, doi:10.3402/tellusa.v10i2.9229, URL https://doi.org/10.3402%2Ftellusa.v10i2.9229.

Stein TH, Westbrook CD, Nicol J. 2015. Fractal geometry of aggregate snowflakes revealed by triple-wavelength radar measurements. *Geophysical Research Letters* **42**(1): 176–183, doi:10.1002/2014gl062170.

Stephens GL. 2005. Cloud Feedbacks in the Climate System: A Critical Review. *J. Climate* **18**(2): 237–273, doi:10.1175/jcli-3243.1, URL http://dx.doi.org/10.1175/JCLI-3243.1.

Stephens GL, Vane DG, Boain RJ, Mace GG, Sassen K, Wang Z, Illingworth AJ, O'Connor EJ, Rossow WB, Durden SL, et al. 2002. THE CLOUDSAT MISSION AND THE A-TRAIN. *Bulletin of the American Meteorological Society* **83**(12): 1771–1790, doi:10.1175/bams-83-12-1771, URL http:

//dx.doi.org/10.1175/bams-83-12-1771.

Tyynela J, Leinonen J, Moisseev D, Nousiainen T. 2011. Radar Backscattering from Snowflakes: Comparison of Fractal, Aggregate, and Soft Spheroid Models. *Journal of Atmospheric and Oceanic Technology* **28**(11): 1365–1372, doi:10.1175/jtech-d-11-00004.1, URL http://dx.doi.org/10.1175/JTECH-D-11-00004.1.

Vié B, Pinty JP, Berthet S, Leriche M. 2016. LIMA (v1.0): A quasi two-moment microphysical scheme driven by a multimodal population of cloud condensation and ice freezing nuclei. *Geoscientific Model Development* **9**(2): 567–586, doi:10.5194/gmd-9-567-2016, URL https://doi.org/10.5194%2Fgmd-9-567-2016.

Wattrelot E, Caumont O, Mahfouf JF. 2014. Operational Implementation of the 1D+3D-Var Assimilation Method of Radar Reflectivity Data in the AROME Model. *Monthly Weather Review* **142**(5): 1852–1873, doi:10.1175/mwr-d-13-00230.1, URL http://dx.doi.org/10.1175/MWR-D-13-00230.1.

Wolde M, Pazmany A. 2005. NRC Dual-Frequency Airborne Radar for Atmospheric Research.

Yuter SE, Houze RA. 1995. Three-Dimensional Kinematic and Microphysical Evolution of Florida Cumulonimbus. Part II: Frequency Distributions of Vertical Velocity, Reflectivity, and Differential Reflectivity. *Monthly Weather Review* **123**(7): 1941–1963, doi:10.1175/1520-0493(1995)123<1941:tdkame>2.0.co;2, URL http://dx.doi.org/10.1175/1520-0493(1995)123<1941:TDKAME>2.0.CO;2.